EDGE ARTICLE

Check for updates

Oxidative control over the morphology of Cu₃(HHTP)₂, a 2D conductive metal–organic framework†

Kathleen M. Snook, [ID] Leo B. Zasada, [ID] Dina Chehada and Dianne J. Xiao [ID] *

The morphology of electrically conductive metal–organic frameworks strongly impacts their performance in applications such as energy storage and electrochemical sensing. However, identifying the appropriate conditions needed to achieve a specific nanocrystal size and shape can be a time-consuming, empirical process. Here we show how partial ligand oxidation dictates the morphology of Cu₃(HHTP)₂ (HHTP = 2,3,6,7,10,11-hexahydroxytriphenylene), a prototypical 2D conductive metal–organic framework. Using organic quinones as the chemical oxidant, we demonstrate that partial oxidation of the ligand prior to metal binding alters the nanocrystal aspect ratio by over 60-fold. Systematically varying the extent of initial ligand oxidation leads to distinct rod, block, and flake-like morphologies. These results represent an important advance in the rational control of Cu₃(HHTP)₂ morphology and motivate future studies into how ligand oxidation impacts the nucleation and growth of 2D conductive metal–organic frameworks.

Introduction

Over the past decade, electrically conductive metal–organic frameworks (MOFs) have grown from a scientific rarity to a rapidly expanding body of materials.[1] As the number of conductive MOF architectures continues to increase, the next synthetic hurdle will be in the realm of morphological control. With respect to device performance, the impact of changing nanocrystal size and shape can be as powerful as altering the underlying molecular structure. Tuning particle morphology to enhance mass transfer has been shown to significantly increase the specific capacitance of MOF-based energy storage devices[2,3] and the sensitivity of MOF-based electrochemical sensors.[4] In addition to higher mass transport rates, downsizing bulk MOFs to form colloidally stable nanocrystals may also provide important processability advantages.[5,6]

This study focuses on controlling the morphology of Cu₃(HHTP)₂ (HHTP = 2,3,6,7,10,11-hexahydroxytriphenylene), a prototypical 2D conductive metal–organic framework (Fig. 1).[7] Cu₃(HHTP)₂ is part of a larger family of isostructural frameworks with varying metal identities (*e.g.*, Fe, Co, Ni, Cu, *etc.*), bridging heteroatoms (O, NH, S), and aromatic cores (*e.g.*, triphenylene, benzene, *etc.*).[1,7–14] Members of this family of frameworks represent some of the most highly conductive metal–organic frameworks reported to date.[1]

Department of Chemistry, University of Washington, Seattle, Washington 98195, USA. E-mail: djxiao@uw.edu

† Electronic supplementary information (ESI) available. See https://doi.org/10.1039/d2sc03648g

Under solvothermal conditions, Cu₃(HHTP)₂ generally crystallizes as thin nanorods, with the long axis in the π-stacking direction.[7,15] The particle aspect ratio can be tuned by varying multiple reaction parameters (*e.g.*, metal precursor, presence of modulators, solvent combination, *etc.*), and rod, block, and aggregated flake-like particles of Cu₃(HHTP)₂ have all been reported.[3,15] Given the large number of reaction variables, identifying appropriate conditions for a given morphology is a time-consuming, empirical process. Furthermore, in our hands, reported literature morphologies have often been irreproducible. Here, we sought to better understand the origins of irreproducibility in Cu₃(HHTP)₂ synthesis, as well as identify which reaction variables have the largest influence on nanocrystal morphology.

An important step towards the rational control of Cu₃(HHTP)₂ nanocrystal morphology is a better understanding of the key reactions involved in framework formation. In contrast to traditional MOFs constructed from redox-inactive building blocks, the synthesis of Cu₃(HHTP)₂ and its structural congeners requires a unique ligand oxidation step (Fig. 1). A growing body of evidence has underscored the importance of aerobic oxidation to framework formation. For example, in the absence of O₂, electron-rich catechol ligands can reduce Cu(ɪɪ) to form Cu(0) nanoparticles.[16] No precipitate is formed during the synthesis of Co₃(HITP)₂ (HITP = 2,3,6,7,10,11-hexaimino-triphenylene) if air is excluded,[17] and continuous air sparging is often required in the scale-up of Ni₃(HITP)₂.[18] Surprisingly, despite the well-established importance of air to the synthesis of Cu₃(HHTP)₂ and other 2D conductive frameworks, ligand oxidation remains a largely understudied reaction parameter. We hypothesized that greater control over the oxidant identity,
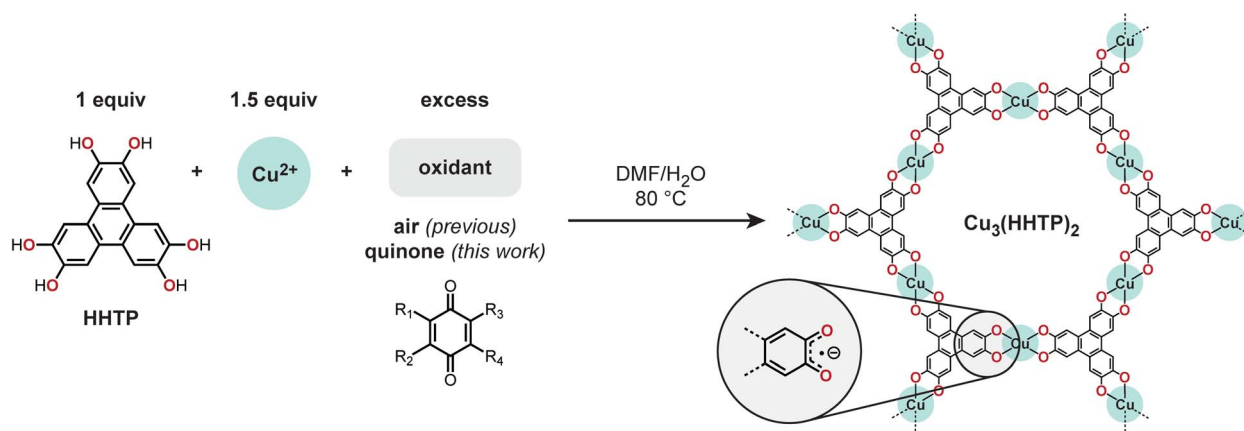
Fig. 1 Overview of $Cu_3(HHTP)_2$ synthesis and structure. The presence of a chemical oxidant is critical to framework formation, as the three catechol units in HHTP must be oxidized by $1\ e^-$ each ($3\ e^-$ per ligand). The synthesis is traditionally performed with air as the oxidant. This work introduces a controlled oxidative synthesis that uses substituted quinones as the chemical oxidant.

stoichiometry, and rate of introduction would provide new insights into how nanocrystal size and shape can be controlled in this class of materials.

Here, we report a new synthetic route to $Cu_3(HHTP)_2$ that uses easy-to-handle solids, specifically quinones, as the chemical oxidant rather than air. With this route, we have discovered that partial oxidation of the HHTP ligand prior to introduction of a metal source dramatically alters the resulting particle morphology. Keeping all other reaction variables constant, tuning the extent of initial ligand oxidation leads to a 60-fold change in the nanocrystal length : diameter aspect ratio. These results represent an important advance in the rational control of $Cu_3(HHTP)_2$ morphology and motivate future studies into how ligand oxidation impacts the nucleation and growth of 2D conductive metal–organic frameworks.

Results and discussion

Ligand purity and synthetic reproducibility

In the synthesis of colloidal semiconductor and metal nanocrystals, it is well-known that trace impurities in the metal precursors, surfactants, and solvents can lead to large changes in nanocrystal shape, size, and polydispersity.[19–21] Therefore, before undertaking a deeper investigation of $Cu_3(HHTP)_2$ nanocrystal formation, we first paused to examine the purity of our reagents. In particular, special attention was paid to the HHTP ligand. This air-sensitive ligand is sold commercially at a relatively low purity level (95%) and is often received as a dark grey to black solid, indicative of oxidation. In the presence of air, catechol-containing compounds are known to undergo darkening as a result of oxidative polymerization and cross-linking, a process that has been exploited in both synthetic and biological systems.[22–26]

The purity of four HHTP samples purchased from two separate suppliers was determined using a combination of thermogravimetric analysis (TGA), quantitative nuclear magnetic resonance (NMR) spectroscopy, and quantitative electron paramagnetic resonance (EPR) spectroscopy (see ESI

for more details).† Significant variation in batch-to-batch purity was observed. Across the four samples, water and HHTP accounted for only 61.5–93.7% of the sample by mass; the remainder was attributed to an NMR and EPR-silent impurity (Table S1 and Fig. S2†). We hypothesized that the impurity could be a polymeric or oligomeric species formed by the oxidative cross-linking of HHTP. Indeed, the presence of extended structures was confirmed by dynamic light scattering (DLS) studies, which showed particles ranging from 200–800 nm in diameter (Table S2†).

Given the significant impurities present in the as-received commercial HHTP ligand, we developed a simple and straightforward method to purify the compound. Oxidized species could be completely removed *via* reduction of the sample with excess $Na_2S_2O_4$ followed by filtration over activated charcoal. The resulting light tan powder was >99% pure by quantitative NMR.

We found that the initial HHTP purity level strongly influences particle morphology. Following previously reported procedures for $Cu_3(HHTP)_2$ nanorods,[15] three batches of the framework were synthesized using three different ligand sources: (1) purified HHTP (>99 wt%), (2) HHTP purchased from TCI Chemicals (81 wt%), and (3) HHTP purchased from Acros (68 wt%). While mixtures of nanorods and intergrown, aggregated particles were obtained in all cases, significant differences in particle diameter were observed (Fig. S4†). Both purified and TCI Chemicals HHTP produced thin nanorods with average diameters of ~90 nm, while the Acros HHTP led to a bimodal distribution of thicker nanorods with diameters centered around ~100 and ~300 nm (Fig. S5†).

Quinone-based synthesis of $Cu_3(HHTP)_2$

The investigations into ligand purity described above show that organic impurities formed by the oxidative polymerization of catechol-containing ligands can be a significant source of irreproducibility in $Cu_3(HHTP)_2$ synthesis. Viewed from a different perspective, these findings also imply that ligand oxidation

could be an important and previously overlooked parameter for controlling particle size and shape. We hypothesized that, when properly controlled, the redox activity of HHTP could serve as a powerful handle for manipulating $Cu_3(HHTP)_2$ nanocrystal morphology.

To evaluate whether oxidative control of $Cu_3(HHTP)_2$ morphology is possible, we first needed a more precise means of controlling oxidant stoichiometry, rate of addition, and oxidizing strength. This motivated us to develop a quinone-based synthesis of $Cu_3(HHTP)_2$ (Fig. 2). Unlike air, quinones are easy-to-handle solids. Furthermore, their 1 e^- reduction potentials can be systematically tuned by >1 V simply by altering the size of the conjugated ring system and the steric and electronic properties of the substituents.[27] Finally, many quinones readily sublime at either ambient or elevated temperatures, giving us the flexibility to choose whether oxidant is added quickly at the start of the reaction or slowly introduced over several hours *via* sublimation.

Using UV-vis spectroscopy, we measured the rate at which four quinones of varying oxidant strength sublimed from a 20 mL scintillation vial into an interior 4 mL vial containing dimethylformamide (Fig. S6 and Table S3†). These studies were carried out at ambient pressure and 80 °C, the standard $Cu_3(HHTP)_2$ synthesis temperature. As depicted in Fig. S6 and Table S3† the rate of sublimation was inversely correlated with the molecular weight of the quinone. For example, under these conditions, 1,4-benzoquinone sublimed with a rate of 9.7 ± 3.9 × 10^{-4} mmol min^{-1}, whereas 2,6-dimethyl-1,4-benzoquinone sublimed with a rate of 1.6 ± 0.2 × 10^{-4} mmol min^{-1} (Table S3†). The sublimation rate of 2,5-dichloro-1,4-benzoquinone was nearly negligible.

Due to their differing sublimation rates and redox potentials, quinones allow us to tune both the rate of oxidant introduction and the overall oxidant strength. To probe how these factors influence nanocrystal morphology, three $Cu_3(HHTP)_2$ syntheses were carried out under an inert atmosphere using 1,4-benzoquinone, 2-methyl-1,4-benzoquinone, or 2,6-dimethyl-1,4-benzoquinone as the oxidant (Fig. 2). In all cases, the quinone was gradually introduced *via* sublimation, using the reaction set

up illustrated in Fig. 2a. The reaction scale was chosen such that at least three equivalents of quinone per HHTP sublimed into the interior reaction vessel over the course of the reaction. After 24 h, phase-pure $Cu_3(HHTP)_2$ was produced in all cases. When the reaction was carried without any oxidant present, diffraction peaks associated with Cu_2O as well as an unidentified secondary phase were observed in addition to $Cu_3(HHTP)_2$ (Fig. S7 and S8†).

Scanning electron microscopy (SEM) images showed that the resulting $Cu_3(HHTP)_2$ nanocrystal morphology and overall sample uniformity strongly depended on the oxidant used. Stronger oxidants with faster sublimation rates, such as 1,4-benzoquinone, led to a complex mixture of individual rod-like particles as well as larger spherical clusters composed of many radially oriented nanocrystals (Fig. 2b). A significant reduction in the number of intergrown aggregates was observed when the milder oxidant 2-methyl-1,4-benzoquinone was used (Fig. 2c). Finally, the weakest oxidant with the slowest sublimation rate, 2,6-dimethyl-1,4-benzoquinone, led to well-defined, rod-like particles with no other competing morphologies or aggregates (Fig. 2d). Based on an analysis of over 250 particles, the rods were 1.15 ± 0.80 μm in length and 0.13 ± 0.05 μm in diameter (Fig. 3b). Importantly, these syntheses were highly reproducible. Similar morphologies were observed across twenty repeat batches.

Impact of ligand pre-oxidation on nanocrystal morphology

After establishing that slow sublimation of a weak quinone oxidant is required to achieve more uniform sample morphologies, we next turned our attention to the effect of ligand impurities. Given that many commercial sources of HHTP contain large quantities of oxidatively cross-linked HHTP, we wanted to rigorously examine the effect of ligand oxidation on $Cu_3(HHTP)_2$ formation.

The amount of oxidized ligand impurities present in solution can be dialed in by treating purified HHTP ligand with varying equivalents of quinone prior to framework synthesis. For these ligand oxidation studies, we used a stronger oxidant, 2,5-dichloro-1,4-benzoquinone, to ensure complete conversion.
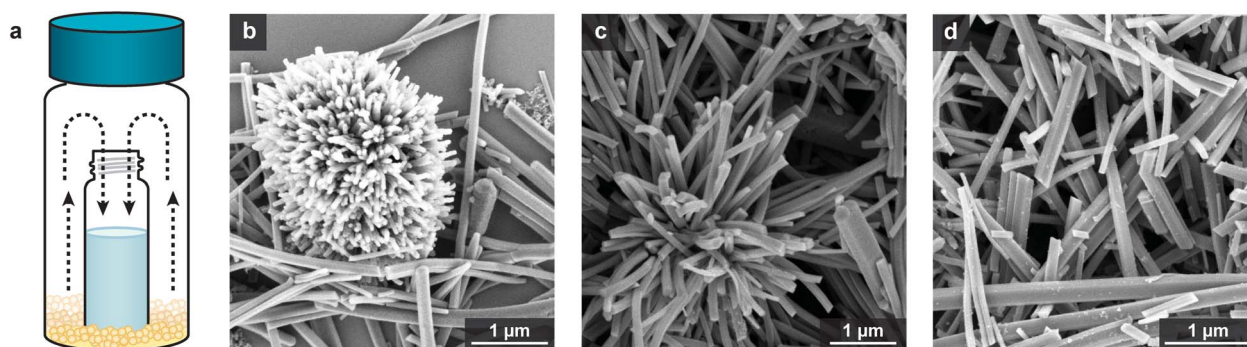

Fig. 2 (a) Standard sublimation reaction set-up. The quinone oxidant is placed in an outer 20 mL vial, whereas the copper salt, HHTP ligand, and solvent are placed in the inner 4 mL vial. As the reaction is heated, the quinone oxidant sublimes into the inner 4 mL vial. (b–d) Scanning electron microscopy images of $Cu_3(HHTP)_2$ prepared with 3 equiv. of (b) 1,4-benzoquinone, (c) 2-methyl-1,4-benzoquinone, and (d) 2,6-dimethyl-1,4-benzoquinone.
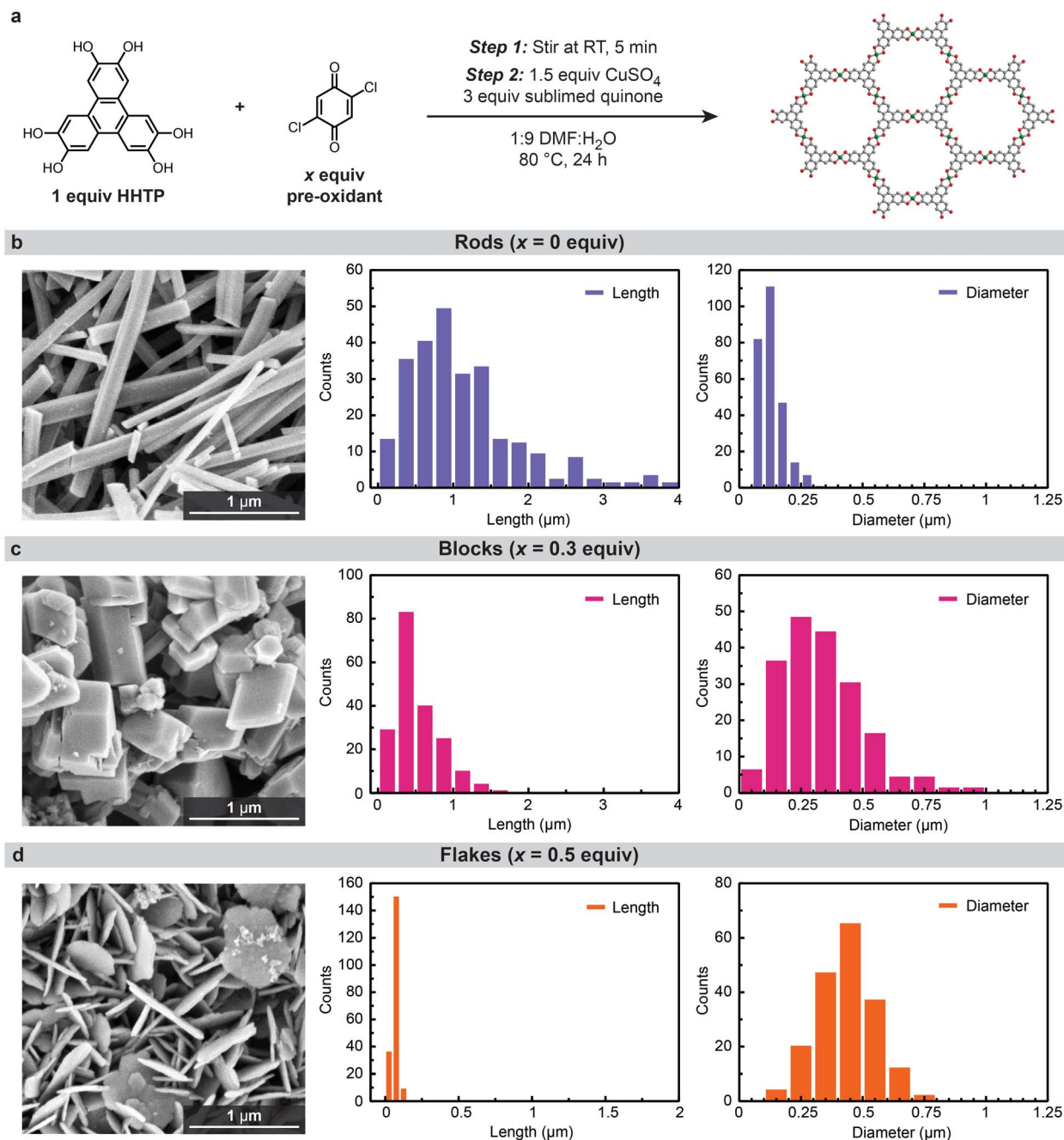
Fig. 3 (a) Overview of two-step $Cu_3(HHTP)_2$ synthesis, consisting of initial ligand pre-oxidation with 2,5-dichloro-1,4-benzoquinone, followed by framework formation. (b–d) Scanning electron microscopy images and length/diameter distributions for $Cu_3(HHTP)_2$ synthesized using (b) 0, (c) 0.3, and (d) 0.5 equivalents of 2,5-dichloro-1,4-benzoquinone as a pre-oxidant. As the equivalents of pre-oxidant increases, three distinct morphologies are observed: narrow, well-defined nanorods; thick, irregular hexagonal particles; and thin, intergrown flakes.

Based on quantitative NMR, EPR, and DLS studies, the impurities formed by treatment of HHTP with 2,5-dichloro-1,4-benzoquinone closely resemble the impurities found in as-received, commercial HHTP. For example, upon addition of 0.3 equiv. of 2,5-dichloro-1,4-benzoquinone, 26.6% of the HHTP ligand becomes NMR silent (Fig. S11†). Only trace radical species were observed by quantitative EPR (<0.1 mol%). Dynamic light scattering studies showed the presence of

polymeric or oligomeric species with broad, bimodal distributions centered around 530 ± 130 and 80 ± 14 nm (Table S2†).

To tease out the impact of oxidized ligand impurities on particle morphology, $Cu_3(HHTP)_2$ was synthesized *via* a two-step procedure composed of (1) ligand pre-oxidation followed by (2) framework formation. In the first step, purified HHTP is dissolved and treated with varying equivalents of 2,5-dichloro-1,4-benzoquinone at room temperature. In the second step, $CuSO_4$ is added to the reaction mixture, the reaction is heated to

80 °C, and additional oxidant (2,6-dimethy-1,4-lbenzoquinone) is slowly introduced *via* sublimation.

While the resulting $Cu_3(HHTP)_2$ samples are somewhat polydisperse, a clear trend between the extent of ligand pre-oxidation and the average length : diameter ratio is observed (Fig. 3). Keeping all other reaction variables constant, tuning the initial extent of ligand oxidation leads to an over 60-fold decrease in the particle aspect ratio, from 8.85 to 0.13. When no 2,5-dichloro-1,4-benzoquinone is added, well-defined $Cu_3(-HHTP)_2$ nanorods with an average length of 1.15 ± 0.80 μm and diameter of 0.13 ± 0.05 μm are observed, as discussed previously (Fig. 3b). Further increasing the amount of 2,5-dichloro-1,4-benzoquinone to 0.3 equiv. produces thick, block-like particles with an average length of 0.55 ± 0.33 μm and diameter of 0.33 ± 0.18 μm (Fig. 3c). Finally, addition of 0.5 equiv. 2,5-dichloro-1,4-benzoquinone pre-oxidant leads to a further reduction in the length dimension as thin, intergrown petal-like flakes are produced (Fig. 3d). These flakes are approximately 0.06 ± 0.02 μm in length and 0.45 ± 0.19 μm in diameter.

Aside from differences in morphology, the three $Cu_3(HHTP)_2$ samples are nearly indistinguishable by all other characterization methods. All three powder X-ray diffraction patterns match that expected for $Cu_3(HHTP)_2$ (Fig. 4a). Similar Brunauer–

Emmett–Teller (BET) surface areas of 560, 540, and 390 m^2 g^{-1} are observed for the rod, block, and flake morphologies, respectively (Fig. 4b). The slightly lower surface area observed for the flake morphology may be a result of its more intergrown nature (Fig. 3d). Nevertheless, all surface area values are consistent with literature values, which generally range between $\sim$300–500 m^2 g^{-1}.[1,28,29] Furthermore, no differences were observed by either infrared spectroscopy (Fig. S18†) or X-ray photoelectron spectroscopy (Fig. S19 and Table S6†). Finally, all materials exhibit conductivity values on the order of 10^{-2} to 10^{-3} S cm^{-1} (Fig. S20 and Table S7†).

The above findings establish a strong connection between the $Cu_3(HHTP)_2$ length : diameter aspect ratio and the extent of ligand oxidative polymerization, a previously overlooked synthetic parameter. The interaction between the oxidized HHTP polymer and the $Cu_3(HHTP)_2$ precursors and crystal surfaces is likely complex. In addition to chelating sites capable of binding to specific facets, the redox-active polymer may also serve as alternative oxidant source during synthesis. While the exact mechanism by which the oxidized HHTP polymer alters $Cu_3(HHTP)_2$ morphology is not yet understood, macromolecular additives are well-known to influence crystal formation.[30] For example, macromolecular additives have been shown to promote the nucleation of many crystal types, including small molecules and zeolites,[31,32] as well as modulate the growth of metal–organic frameworks.[33–35] Future work will focus on elucidating the structure of oxidized HHTP, and *in situ* studies to better understand how the polymer impacts nucleation and growth.

Conclusions

In conclusion, we have developed a new synthesis of $Cu_3(-HHTP)_2$ that relies on organic quinones rather than air as the oxidant. Unlike air, quinones are easy-to-handle solids, allowing the rate and timing of oxidant addition, as well as the overall oxidant stoichiometry, to be carefully tuned. Using this new synthetic route, we have shown how the controlled oxidative polymerization of HHTP can serve as a powerful tool to manipulate $Cu_3(HHTP)_2$ morphology. By varying the extent of initial ligand oxidation, we can achieve diverse rod, block, and flake-like morphologies. While more work is needed to understand the exact structure and role of the polymeric species formed upon ligand oxidation, we hypothesize that these species may serve as coordination modulators or oxidant reservoirs. Finally, our work highlights the importance of reagent purity on the reproducibility of metal–organic framework nanocrystal synthesis. Future work will focus on understanding the role of oxidized HHTP and determining whether these findings can be generalized to other members of this class of conductive 2D metal–organic frameworks.
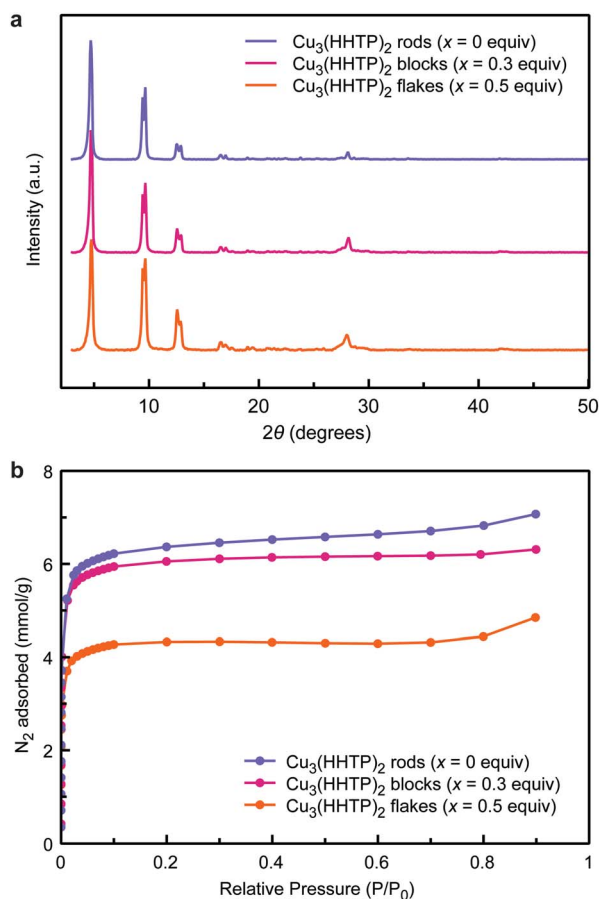

Fig. 4 (a) Powder X-ray diffraction patterns and (b) surface areas of $Cu_3(HHTP)_2$ synthesized with 0, 0.3, and 0.5 equiv. of 2,5-dichloro-1,4-benzoquinone pre-oxidant.

Data availability

Additional experimental data supporting this article are included in the ESI.†

Author contributions

K. M. S. and D. J. X. designed the research. K. M. S. performed the $Cu_3(HHTP)_2$ synthesis and characterization. K. M. S. performed and analyzed ligand oxidation and sublimation experiments. K. M. S. and D. C. developed and performed the ligand purification. L. B. Z. assisted with collecting and fitting electron paramagnetic resonance spectra; K. M. S. prepared and analyzed electron paramagnetic resonance samples. All authors interpreted the results and contributed to the writing of the manuscript.

Conflicts of interest

There are no conflicts to declare.

Acknowledgements

Notes and references

1 L. S. Xie, G. Skorupskii and M. Dincă, Electrically Conductive Metal–Organic Frameworks, *Chem. Rev.*, 2020, **120**(16), 8536–8580, DOI: **10.1021/acs.chemrev.9b00766**.

2 M. A. Borysiewicz, J.-H. Dou, I. Stassen and M. Dincă, Why Conductivity Is Not Always King – Physical Properties Governing the Capacitance of 2D Metal–Organic Framework-Based EDLC Supercapacitor Electrodes: A $Ni_3(HITP)_2$ Case Study, *Faraday Discuss.*, 2021, **231**, 298–304, DOI: **10.1039/D1FD00028D**.

3 J. W. Gittins, C. J. Balhatchet, S. M. Fairclough and A. C. Forse, Enhancing the Energy Storage Performances of Metal–Organic Frameworks by Controlling Microstructure, *Chem. Sci.*, 2022, **13**, 9210–9219, DOI: **10.1039/D2SC03389E**.

4 C.-S. Liu, J. Li and H. Pang, Metal-Organic Framework-Based Materials as an Emerging Platform for Advanced Electrochemical Sensing, *Coord. Chem. Rev.*, 2020, **410**, 213222, DOI: **10.1016/j.ccr.2020.213222**.

5 C. R. Marshall, J. P. Dvorak, L. P. Twight, L. Chen, K. Kadota, A. B. Andreeva, A. E. Overland, T. Ericson, A. F. Cozzolino and C. K. Brozek, Size-Dependent Properties of Solution-Processable Conductive MOF Nanocrystals, *J. Am. Chem. Soc.*, 2022, **144**(13), 5784–5794, DOI: **10.1021/jacs.1c10800**.

6 L. B. Zasada, L. Guio, A. A. Kamin, D. Dhakal, M. Monahan, G. T. Seidler, C. K. Luscombe and D. J. Xiao, Conjugated Metal–Organic Macrocycles: Synthesis, Characterization, and Electrical Conductivity, *J. Am. Chem. Soc.*, 2022, **144**(10), 4515–4521, DOI: **10.1021/jacs.1c12596**.

7 M. Hmadeh, Z. Lu, Z. Liu, F. Gándara, H. Furukawa, S. Wan, V. Augustyn, R. Chang, L. Liao, F. Zhou, E. Perre, V. Ozolins, K. Suenaga, X. Duan, B. Dunn, Y. Yamamto, O. Terasaki and O. M. Yaghi, New Porous Crystals of Extended Metal-Catecholates, *Chem. Mater.*, 2012, **24**(18), 3511–3513, DOI: **10.1021/cm301194a**.

8 D. Sheberla, L. Sun, M. A. Blood-Forsythe, S. Er, C. R. Wade, C. K. Brozek, A. Aspuru-Guzik and M. Dincă, High Electrical Conductivity in Ni3(2,3,6,7,10,11-Hexaiminotriphenylene)2, a Semiconducting Metal–Organic Graphene Analogue, *J. Am. Chem. Soc.*, 2014, **136**(25), 8859–8862, DOI: **10.1021/ja502765n**.

9 A. J. Clough, J. W. Yoo, M. H. Mecklenburg and S. C. Marinescu, Two-Dimensional Metal–Organic Surfaces for Efficient Hydrogen Evolution from Water, *J. Am. Chem. Soc.*, 2015, **137**(1), 118–121, DOI: **10.1021/ja5116937**.

10 T. Kambe, R. Sakamoto, K. Hoshiko, K. Takada, M. Miyachi, J.-H. Ryu, S. Sasaki, J. Kim, K. Nakazato, M. Takata and H. Nishihara, π-Conjugated Nickel Bis(Dithiolene) Complex Nanosheet, *J. Am. Chem. Soc.*, 2013, **135**(7), 2462–2465, DOI: **10.1021/ja312380b**.

11 J. Park, A. C. Hinckley, Z. Huang, D. Feng, A. A. Yakovenko, M. Lee, S. Chen, X. Zou and Z. Bao, Synthetic Routes for a 2D Semiconductive Copper Hexahydroxybenzene Metal–Organic Framework, *J. Am. Chem. Soc.*, 2018, **140**(44), 14533–14537, DOI: **10.1021/jacs.8b06666**.

12 N. Lahiri, N. Lotfizadeh, R. Tsuchikawa, V. V. Deshpande and J. Louie, Hexaaminobenzene as a Building Block for a Family of 2D Coordination Polymers, *J. Am. Chem. Soc.*, 2017, **139**(1), 19–22, DOI: **10.1021/jacs.6b09889**.

13 D. Feng, T. Lei, M. R. Lukatskaya, J. Park, Z. Huang, M. Lee, L. Shaw, S. Chen, A. A. Yakovenko, A. Kulkarni, J. Xiao, K. Fredrickson, J. B. Tok, X. Zou, Y. Cui and Z. Bao, Robust and Conductive Two-Dimensional Metal–organic Frameworks with Exceptionally High Volumetric and Areal Capacitance, *Nat. Energy*, 2018, **3**(1), 30–36, DOI: **10.1038/s41560-017-0044-5**.

14 H. T. B. Pham, J. Y. Choi, S. Huang, X. Wang, A. Claman, M. Stodolka, S. Yazdi, S. Sharma, W. Zhang and J. Park, Imparting Functionality and Enhanced Surface Area to a 2D Electrically Conductive MOF via Macrocyclic Linker, *J. Am. Chem. Soc.*, 2022, 2c03793, DOI: **10.1021/jacs.2c03793**.

15 R. W. Day, D. K. Bediako, M. Rezaee, L. R. Parent, G. Skorupskii, M. Q. Arguilla, C. H. Hendon, I. Stassen, N. C. Gianneschi, P. Kim and M. Dinca, Single Crystals of

Electrically Conductive Two-Dimensional Metal-Organic Frameworks: Structural and Electrical Transport Properties, *ACS Cent. Sci.*, 2019, **5**(12), 1959–1964, DOI: 10.1021/acscentsci.9b01006.

16 Y. Jiang, I. Oh, S. H. Joo, Y.-S. Seo, S. H. Lee, W. K. Seong, Y. J. Kim, J. Hwang, S. K. Kwak, J.-W. Yoo and R. S. Ruoff, Synthesis of a Copper 1,3,5-Triamino-2,4,6-Benzenetriol Metal–Organic Framework, *J. Am. Chem. Soc.*, 2020, 0c02389, DOI: 10.1021/jacs.0c02389.

17 T. Chen, J. Dou, L. Yang, C. Sun, N. Libretto, G. Skorupskii, J. T. Miller and M. Dinca, Continuous Electrical Conductivity Variation in M3(Hexaiminotriphenylene)2 (M = Co, Ni, Cu) MOF Alloys, *J. Am. Chem. Soc.*, 2020, 0c04458, DOI: 10.1021/jacs.0c04458.

18 D. Sheberla, J. C. Bachman, J. S. Elias, C.-J. Sun, Y. Shao-Horn and M. Dincă, Conductive MOF Electrodes for Stable Supercapacitors with High Areal Capacitance, *Nat. Mater.*, 2017, **16**(2), 220–224, DOI: 10.1038/nmat4766.

19 X. Peng, L. Manna, W. Yang, J. Wickham, E. Scher, A. Kadavanich and A. P. Alivisatos, Shape Control of CdSe Nanocrystals, *Nature*, 2000, **404**(6773), 59–61, DOI: 10.1038/35003535.

20 D. K. Smith and B. A. Korgel, The Importance of the CTAB Surfactant on the Colloidal Seed-Mediated Synthesis of Gold Nanorods, *Langmuir*, 2008, **24**(3), 644–649, DOI: 10.1021/la703625a.

21 L. M. Liz-Marzán, C. R. Kagan and J. E. Millstone, Reproducibility in Nanocrystal Synthesis? Watch Out for Impurities, *ACS Nano*, 2020, **14**(6), 6359–6361, DOI: 10.1021/acsnano.0c04709.

22 N. Patil, C. Jérôme and C. Detrembleur, Recent Advances in the Synthesis of Catechol-Derived (Bio)Polymers for Applications in Energy Storage and Environment, *Prog. Polym. Sci.*, 2018, **82**, 34–91, DOI: 10.1016/j.progpolymsci.2018.04.002.

23 J. Yang, M. A. Cohen Stuart and M. Kamperman, Jack of All Trades: Versatile Catechol Crosslinking Mechanisms, *Chem. Soc. Rev.*, 2014, **43**(24), 8271–8298, DOI: 10.1039/C4CS00185K.

24 S. Sánchez-Cortés, O. Francioso, J. V. García-Ramos, C. Ciavatta and C. Gessa, Catechol Polymerization in the Presence of Silver Surface, *Colloids Surf., A*, 2001, **176**(2–3), 177–184, DOI: 10.1016/S0927-7757(00)00630-0.

25 G. Yan, G. Chen, Z. Peng, Z. Shen, X. Tang, Y. Sun, X. Zeng and L. Lin, The Cross-Linking Mechanism and Applications of Catechol–Metal Polymer Materials, *Adv. Mater. Interfaces*, 2021, **8**(19), 2100239, DOI: 10.1002/admi.202100239.

26 H. Lee, S. M. Dellatore, W. M. Miller and P. B. Messersmith, Mussel-Inspired Surface Chemistry for Multifunctional Coatings, *Science*, 2007, **318**(5849), 426–430, DOI: 10.1126/science.1147241.

27 M. T. Huynh, C. W. Anson, A. C. Cavell, S. S. Stahl and S. Hammes-Schiffer, Quinone 1 e^- and 2 e^-/2 H^+ Reduction Potentials: Identification and Analysis of Deviations from Systematic Scaling Relationships, *J. Am. Chem. Soc.*, 2016, **138**(49), 15903–15910, DOI: 10.1021/jacs.6b05797.

28 M. de Lourdes Gonzalez-Juarez, E. Flores, M. Martin-Gonzalez, I. Nandhakumar and D. Bradshaw, Electrochemical Deposition and Thermoelectric Characterisation of a Semiconducting 2-D Metal–Organic Framework Thin Film, *J. Mater. Chem. A*, 2020, **8**(26), 13197–13206, DOI: 10.1039/D0TA04939E.

29 J. W. Gittins, C. J. Balhatchet, Y. Chen, C. Liu, D. G. Madden, S. Britto, M. J. Golomb, A. Walsh, D. Fairen-Jimenez, S. E. Dutton and A. C. Forse, Insights into the Electric Double-Layer Capacitance of Two-Dimensional Electrically Conductive Metal–Organic Frameworks, *J. Mater. Chem. A*, 2021, **9**(29), 16006–16015, DOI: 10.1039/D1TA04026J.

30 A. G. Shtukenberg, M. D. Ward and B. Kahr, Crystal Growth with Macromolecular Additives, *Chem. Rev.*, 2017, **117**(24), 14042–14090, DOI: 10.1021/acs.chemrev.7b00285.

31 L. Y. Pfund, C. P. Price, J. J. Frick and A. J. Matzger, Controlling Pharmaceutical Crystallization with Designed Polymeric Heteronuclei, *J. Am. Chem. Soc.*, 2015, **137**(2), 871–875, DOI: 10.1021/ja511106j.

32 H. Dai, J. Claret, E. L. Kunkes, V. Vattipalli, N. Linares, C. Huang, M. Fiji, J. García-Martinez, A. Moini and J. D. Rimer, Accelerating the Crystallization of Zeolite SSZ-13 with Polyamines, *Angew. Chem., Int. Ed.*, 2022, **61**(16), e202117742, DOI: 10.1002/anie.202117742.

33 M. Kalaj, K. C. Bentz, S. Ayala, J. M. Palomba, K. S. Barcus, Y. Katayama and S. M. Cohen, MOF-Polymer Hybrid Materials: From Simple Composites to Tailored Architectures, *Chem. Rev.*, 2020, **120**(16), 8267–8302, DOI: 10.1021/acs.chemrev.9b00575.

34 T. Uemura, Y. Hoshino, S. Kitagawa, K. Yoshida and S. Isoda, Effect of Organic Polymer Additive on Crystallization of Porous Coordination Polymer, *Chem. Mater.*, 2006, **18**(4), 992–995, DOI: 10.1021/cm052427g.

35 T.-H. Chen, L. Wang, J. V. Trueblood, V. H. Grassian and S. M. Cohen, Poly(Isophthalic Acid)(Ethylene Oxide) as a Macromolecular Modulator for Metal–Organic Polyhedra, *J. Am. Chem. Soc.*, 2016, **138**(30), 9646–9654, DOI: 10.1021/jacs.6b04971.